CALPHAD: Computer Coupling of Phase Diagrams and Thermochemistry 76 (2022) 102365

Contents lists available at ScienceDirect

Calphad

journal homepage: www.elsevier.com/locate/calphad

Kinetic interface condition phase diagram for the rapid solidification of multi-component alloys with an application to additive manufacturing

Qiang Du *, Amin S. Azar, Mohammed M'Hamdi

SINTEF Industry, Oslo, Norway

ARTICLE INFO

Keywords:
Kinetic interface condition
Rapid solidification
Solute drag
Growth restriction factor
Additive manufacturing

ABSTRACT

Solid-liquid Interface response function or the analysis of kinetic interfacial conditions under rapid solidification setting occupies a central role in solidification research. With the concepts of solute drag and solute trapping and on the base of irreversible thermodynamics, the calculation of kinetic interface condition phase diagram for binary alloys has been well established owing to the continuous growth model by Aziz et al. Motivated by the fast development of various additive manufacturing (AM) technologies, clear needs to extend the kinetic phase diagram calculation towards multi-component alloy systems emerge to meet the challenges of processing parameter optimization encountered under those sub-rapid or rapid AM solidification conditions for new alloys. In this paper the irreversible thermodynamics analysis and the binary continuous growth model are reformulated into a form suitable for the coupling with the multi-component CALPHAD databases. Then the numerical solution to the CALPHAD-coupled multi-component model is described. The model and its numerical solution are verified by comparing its calculation results with those reported in literature for A-B hypothetical ideal solution phases, Ag–Cu and Al–Be alloys. The model predictive power is demonstrated by calculating the kinetic diagram of Al–Ti, Fe–Cr–Ni and Al–Cu–Mg–Si–Zn alloys. To illustrate one of the practical values of the proposed model, kinetic growth restriction factor is calculated from the predicted Al–Ti and Al–Cu–Mg–Si–Zn kinetic phase diagram. It is concluded that the proposed multi-component model and its numerical solution can calculate kinetic phase diagram of any multi-component alloys. Moreover, the proposed model can be used in evaluating solute effect for grain refinement under sub-rapid or rapid solidification conditions, which is great value to understand the solidification phenomenon in AM. The model is expected to be useful in many scenarios to guide the optimization of AM processing parameters and alloys design.

1. Introduction

When the interface separating a liquid (parent) and solid (product) phase moves at high velocity, solute drag and solute trapping cause its deviation from thermodynamic equilibrium [1–3]. The interface response to the fast interface migration or the analysis of kinetic interfacial conditions occupies a central role in the study of solidification as well as solid state phase transformation. Kinetic interface condition phase diagrams are often referred for interpreting the formation of the solidification microstructure or optimization of processing parameters under sup-rapid and rapid solidification condition. While research efforts on this kinetic phase diagram calculation had guided the discoveries of a rich spectrum of new metallic materials such as metallic glass, a revisit is to be made in this article to address the thermodynamic and kinetic factors in multi-component alloys that dictate the evolution of microstructure under the rapid cooling condition relevant to additive manufacturing, i.e., the cooling rates that reach up to 10^7 K/s [4–8].

The interface response function for phase transformation is built on irreversible thermodynamics [2]. As summarized by Hillert [3], there are two independent Gibbs energy dissipation process at the interface. The first one is for structural change, i.e., crystallization (in case of solidification) or lattice transforms (in case of solid-state phase transformation), and the second one is for compositional change, i.e., *trans*-interface diffusion. To identify the driving forces for the two processes and relations between the driving forces and their congruent fluxes, various models have been proposed, among which the continuous growth model by Aziz et al. [1] and linear kinetic relations by Hillert, Agren and Liu [3,9,10] have been widely used. The diffusive interface model, i.e. phase field method, have also been applied to study interface response [11–15] under rapid or sub-rapid solidification

* Corresponding author.
E-mail address: qiang.du@sintef.no (Q. Du).

https://doi.org/10.1016/j.calphad.2021.102365
Received 31 July 2021; Received in revised form 4 November 2021; Accepted 10 November 2021
Available online 19 November 2021

conditions while the continuous growth model has been used to verify the numerical parameters in those diffusive interface models. Aziz's model is predictive and insightful. Ludwig has attempted to find an analytical solution to the multi-component Aziz model, and concluded that for non-dilute binary and any arbitrary multi-component alloy systems it is not possible to yield an analytical expression for the interface temperature and velocity relation [16]. However numerical solution exists, and Aziz's model remains to be extended for multi-component kinetic phase diagram calculation. The objective of this article is to propose such an extension.

Aziz's model is tightly linked to Hillert-Agren-Liu linear kinetic model for solid state phase transformation [3,9,10]. It is worth clarifying the differences between Aziz's model and the linear kinetic model to put our multi-component extension attempt within the broader context of phase transformation. While Aziz's continuous growth model [1] has the same approach as the linear kinetic model in correlating the phase transformation driving force and chemical potentials, they proposed different relations between driving forces and interface velocity. Aziz and his co-authors used the continuous growth mechanism, which had been used in relating the velocity in a single-component system to the driving force at an "atomically rough" interface [1,17]. The continuous growth model has the following form:

$$v = v_0\left(1 - \exp\left(-\frac{\Delta G_{eff}}{RT}\right)\right) \tag{1a}$$

Where v_0 is the maximum speed of crystal growth at infinite driving force, ΔG_{eff} (defined to be positive here during solidification) is the effective free energy difference between liquid and solid, whose exact nature depends on how the solute drag is treated [17], R is gas constant and T is temperature. Eq. (1)a's first order expansion at small driving forces is in the linear form used by the linear kinetic model, which is:

$$v = \frac{v_0}{RT}\Delta G_{eff} = M\Delta G_{eff} \tag{1b}$$

in which M is mobility.

Depending on the way ΔG_{eff} is taken, as to be summarized in Model Description Section, Aziz's model has two version: with and without solute drag [17]. As pointed out by Hillert, the model with solute drag has the same root as Hillert's model [3]. However the one without solute drag seemed to be supported by the rapid solidification experiments [18,19] and have attracted more following research efforts in solidification research community [16,20,21]. Of course, different models produce different kinetic interface condition phase diagrams. It is experimental results that should be counted on to verify which drag mode produces the "correct" kinetic phase diagram. For the equation governing solute redistribution energy, Aziz and Hillert's treatments also differ in a similar fashion. Approximately Aziz's equation is in exponential form with its first order expansion being the linear form of Hillert's model [3].

Aziz and Kaplan [1] have demonstrated how the binary phase diagram can be calculated numerically, yet, the extension to multi-component alloys have not been made. With the linear kinetic laws between the driving energies for interface migration and *trans*-interface diffusion, Hillert has demonstrated how to construct the dissipated energies from the phase compositions with the molar Gibbs energy graphs of the parent and product phases for a binary alloy as illustrated in Fig. 4 of [3]. Of course, Hillert's dissipated energies construction can produce phase compositions, i.e., the tie-line of a binary kinetic phase diagram, from given values of dissipated energies. For a binary alloy, Aziz and Boettiger have demonstrated that the kinetic phase diagram are analytically attainable with the assumptions of binary dilute solution phases and straight-line solidus/liquidus [17]. The analytical solution is instructive and has even been applied to each solute in a multi-component alloy [22,23]. However, as concluded originally by Aziz et al. in Ref. [17], the solution falls short when these idealistic assumptions are not met. As mentioned above, for non-dilute binary and any arbitrary multi-component alloy systems an analytical solution to Aziz model can not be obtained [15].

Aziz's binary model is extendable toward multi-component alloys. On the other hand, given the rapid progress in the development of thermodynamic databases in the past several decades, it is justifiable to explore the coupling of the continuous growth model with those multi-component thermodynamic databases available in CALPHAD community. It would enable the generation of accurate kinetic interface condition phase diagrams for any alloy systems, which is of a great value for the understanding of thermodynamic and kinetic mechanisms that dictate the evolution of microstructure under additive manufacturing or any other rapid cooling or phase transformation conditions. The calculation of the kinetic phase diagram would also enable the further extension of the numerical model built on local equilibrium assumption such as the ones reported in Refs. [24,25] or on quasi-equilibrium assumption used in phase field method [26], to non-equilibrium conditions by simply replacing the equilibrium phase diagram with the velocity-dependent phase diagram. Instead of setting the interfacial compositions, i.e., the boundary conditions for each solute diffusion equation in the bulk phases, with the data from the equilibrium phase diagram, the data from kinetic interface condition phase diagram are provided. The boundaries conditions would not be Dirichlet type as they are dependent on the unknown interface velocity, i.e., the derivatives of the solute composition field, and must be solved together with those diffusion equations. These numerical complexities are treatable with the existing numerical algorithm used to solve the moving boundary diffusion problem. In addition, the kinetic phase diagram calculation would provide steady state solutions to verify the non-equilibrium phase transformation models [21,27] that have taken into consideration both diffusion inside the interface and in the bulk phase.

In this article we set out to extend Aziz's continuous growth model to multi-component alloys and couple it with CALPHAD databases. We start with the reformulation of the continuous growth model into a form suitable for the coupling with CALPHAD databases. Then a numerical method for solving the CALPHAD-coupled model is described. The model is applied to ideal solution phases, Ag–Cu, Al–Be, Al–Ti alloys, Fe–Cr–Ni and Al–Cu–Mg–Si–Zn alloys. Some of the binary results are compared with the ones reported in the literature, and the rest serves as the demonstration of the model's behaviour and potential values for the alloys relevant to additive manufacturing.

2. Model description

This section starts with a brief description of the driving force and chemical potential relations derived within the irreversible thermodynamic framework. Then it proceeds to reformulate the relations into the ones amiable to the coupling with multi-component CALPHAD databases. In Section 2.2, the various relations proposed by Aziz et el. between the driving force and interface velocity are revisited to come up with a generic formulation for multi-component alloys. Finally, a numerical algorithm to solve the CALPHAD-coupled multi-component model is described in Section 2.3.

2.1. The relations between driving forces and molar Gibbs energy for a multi-component alloy

As originally reported by Baker and Cahn [2] and Aziz and Kaplan [1], according to irreversible thermodynamics, the following relations between chemical potentials and the molar driving free energy for solidification, ΔG_{DF}, at a migrating solid-liquid interface can be written for a binary alloy consisting of component 1 and component 2:

$$\Delta G_{DF} = \left(X_1^S\Delta\mu_1 + X_2^S\Delta\mu_2\right) \tag{2a}$$

Where $\Delta\mu_j = \mu_j^L - \mu_j^S$ is the chemical potential difference between the liquid and solid at the interface, X_j^S the composition of component j (in

atomic fraction) in solid with the constraint of $X_1^S + X_2^S = 1$. ΔG_{DF} is defined to be positive when solidification occurs. Note that all the driving energy terms depend on temperature and composition, and for clarity the independent variables of temperature and compositions are not explicitly written out.

For n-component alloys, it is straightforward to write:

$$\Delta G_{DF} = \sum_{j=1}^{n} X_j^S \Delta\mu_j \tag{2b}$$

$$\sum_{j=1}^{n} X_j^S = 1 \tag{2c}$$

Let us examine how ΔG_{DF} is spent. For a binary alloy ΔG_{DF} is consumed by two separate processes, one is for driving the interface migration (crystallization) and the other for solute redistribution between component 2 and 1. Therefore, ΔG_{DF} can be written as the sum of crystallization free energy and solute redistribution free energy:

$$\Delta G_{DF} = \Delta G_C + \Delta G_D \tag{3}$$

From kinetic consideration ΔG_C and ΔG_D depend on the interface velocity, v, and this dependency is the topic of Section 2.2. In this section, we restrict ourselves to the thermodynamic relations between driving force and molar Gibbs energies (or chemical potentials) of the liquid and solid phase. According to irreversible thermodynamics:

$$\Delta G_C = \left(X_1^L \Delta\mu_1 + X_2^L \Delta\mu_2\right) \tag{4a}$$

$$\Delta G_D = \left(X_2^L - X_2^S\right)(\Delta\mu_1 - \Delta\mu_2) \tag{4b}$$

$$X_1^L + X_2^L = 1 \tag{4c}$$

For an n-component alloy with component 1 being the major constitution of the alloy, the exchanges among non-major components are ignored. It should be noted that ignoring these changes are based on purely from statistical consideration, i.e., the chances at which solute atoms exchange with the major element atoms over the chances at which they exchange with other alloying elements is equal to their composition ratio, and small in dilute alloys or the alloys with a dominant major substitutional element. However, it shall be noted that these exchanges may become important and shall be considered in some multi-component alloys. With this simplification, ΔG_{DF} is associated with n solute exchange processes between component j and 1 where $j \geq 2$:

$$\Delta G_{DF}(v) = \Delta G_C(v) + \sum_{j=2}^{n} \Delta G_D^j(v) \tag{5}$$

ΔG_C and ΔG_D can be written as:

$$\Delta G_C = \sum_{j=1}^{n} X_j^L \Delta\mu_j \tag{6a}$$

$$\Delta G_D^i = \left(X_i^L - X_i^S\right)(\Delta\mu_1 - \Delta\mu_i)\ i \in (2, n) \tag{6b}$$

$$\sum_{j=1}^{n} X_j^L = 1 \tag{6c}$$

As mentioned earlier, the relationship between ΔG_C and ΔG_D^j to v will be discussed in Section 2.2. An extreme case is that both of ΔG_C and ΔG_D^j are zero when interface moves at negligible velocities, and it is trivial to see that the above equation degenerate to the well-known equal chemical potential conditions used for equilibrium phase diagram calculation, i.e., $\Delta\mu_1 = \Delta\mu_2 = \ldots = \Delta\mu_j = \ldots = \Delta\mu_n = 0$.

To reformulate Eq. (6) into a form amiable to the coupling with CALPHAD database, recall the following relations:

$$G_m^S = \left(1 - \sum_{j=2}^{n} X_j^S\right)\mu_1^S + \sum_{j=2}^{n} X_j^S \mu_j^S \tag{7a}$$

$$G_m^L = \left(1 - \sum_{j=2}^{n} X_j^L\right)\mu_1^L + \sum_{j=2}^{n} X_j^L \mu_j^L \tag{7b}$$

$$\left(\frac{\partial G_m^S}{\partial X_j^S}\right)_{T, X_k^S} = \mu_j^S - \mu_1^S \tag{7c}$$

$$\left(\frac{\partial G_m^L}{\partial X_j^L}\right)_{T, X_k^L} = \mu_j^L - \mu_1^L \tag{7d}$$

The partial derivatives in Eq. (7c) and Eq. (7d) are with respect to solid and liquid phase composition j while the other independent variables, namely T and the compositions of all alloying component other than j being held constant.

With Eq. (7) Eq. (6) can be converted into the following form:

$$\Delta G_C = G_m^L - G_m^S - \sum_{j=2}^{n}\left(X_j^L - X_j^S\right)\left(\frac{\partial G_m^S}{\partial X_j^S}\right)_{T, X_k^S} \tag{8a}$$

$$\Delta G_D^i = \left(X_i^L - X_i^S\right)\left(\left(\frac{\partial G_m^S}{\partial X_i^S}\right)_{T, X_k^S} - \left(\frac{\partial G_m^L}{\partial X_i^L}\right)_{T, X_k^L}\right)\ i \in (2, n) \tag{8b}$$

Rearrange Eq. (8), and substitute Eq. (8b) and Eq. (5) into Eq. (8a), the following form can be written:

$$G_m^S = G_m^L + \sum_{j=2}^{n}\left(X_j^S - X_j^L\right)\left(\frac{\partial G_m^L}{\partial X_j^L}\right)_{T, X_k^L} - \Delta G_{DF}(v) \tag{9a}$$

$$\left(\frac{\partial G_m^S}{\partial X_i^S}\right)_{T, X_k^S} = \left(\frac{\partial G_m^L}{\partial X_i^L}\right)_{T, X_k^L} + \frac{\Delta G_D^i}{X_i^L - X_i^S}\ i \in (2, n) \tag{9b}$$

The differential form of Eq. (9) will be used to calculate kinetic interface condition phase diagram.

The binary forms of Eq. (9a) and Eq. (9b) reflect Hillert's molar Gibbs energy diagram for interfacial compositions (tie-line) construction (Fig. 4 of Ref. [3]). It is worth noting that although the naming convention used for the driving forces is only linked to solute drag model, Eq. (9) is valid for any drag mode, and it does not rely on any assumption on how the driving forces is related to interface velocity.

Similar mathematical forms of Eq. (8) had been derived earlier to calculate Gibbs-Thomson phase diagram [28] and track multi-phase boundaries of general phase diagrams [29]. As demonstrated in Ref. [28], it is straightforward to include the curvature contribution in Eq. (9a) so that Gibbs-Thomson effect on interfacial conditions can be evaluated together with the kinetic contributions. The ability of handing curvature effect and kinetic effect concurrently is important in understanding solidification microstructure formation and solid-state phase transformation. This is considered beyond the scope of this article and will be pursued in a future work.

2.2. The relation between driving forces and interface velocity

In this section, we will describe how the driving force term, i.e, ΔG_C and ΔG_D^j are related to interface velocity. First, we will revisit the continuous growth models with solute drag, without solute drag and mixed mode drag by Aziz et al. [1,17].

Aziz's models are based on chemical rate theory. For the model without solute drag, the overall molar driving free energy is related to the velocity via:

$$\Delta G_{DF} = -RT\ln\left(1-\frac{v}{v_0}\right) \tag{10a}$$

where v_0 is the maximum speed of crystal growth at infinite driving force. Note that in this article the overall driving forces are defined as positive when solidification occur. According to Eq. (5),

$$\Delta G_C = \Delta G_{DF} - \sum_{j=2}^{n}\Delta G_D^j(v) = -RT\ln\left(1-\frac{v}{v_0}\right) - \sum_{j=2}^{n}\Delta G_D^j(v) \tag{10b}$$

In the solute drag model, the crystallization energy is only one part of ΔG_{DF}, i.e., ΔG_C. The other part of ΔG_{DF} is consumed in driving the solute-solvent redistribution reaction. It is ΔG_C that is related to interface velocity via:

$$\Delta G_C = -RT\ln\left(1-\frac{v}{v_0}\right) \tag{11}$$

To unify the two versions of the CGM model, a drag parameter, β, has been defined by Aziz and Boettinger [17], so that

$$\Delta G_{DF}(v) = -RT\ln\left(1-\frac{v}{v_0}\right) + \beta\sum_{j=2}^{n}\Delta G_D^j(v) \tag{12}$$

Unity value of β is for the case that includes solute drag and zero value of β is for the case where no solute drag is present. As pointed out in Ref. [17], the physical meaning of the drag parameter is related to material compositions transferred across the interface.

While ΔG_{DF} and ΔG_D are always larger than zero, ΔG_C might be less than zero in the no drag model according to Eq. (10b). This is in conflict with the analysis made by Hillert [3] on the possible range of the product phase. Hillert's analysis was built on the assumption that crystallization and *trans*-interface diffusion are internal processes so that their driving force must be positive to proceed spontaneously. This conflict has been reconciled by Gurtin and Voorhees [20], stating that the interface is not a close thermodynamic system but the one with external exchange of solute atoms via bulk diffusion from its adjacent layers in the two bulk phases.

$$\left(\frac{\partial G_m^S}{\partial T}-\frac{\partial G_m^L}{\partial T}+\frac{\partial \Delta G_{DF}}{\partial T}-\sum_{j=2}^{n}\left(X_j^S-X_j^L\right)\frac{\partial^2 G_m^L}{\partial X_j^L\partial T}\right)dT+\sum_{j=2}^{n}\left(\frac{\partial G_m^S}{\partial X_j^S}-\frac{\partial G_m^L}{\partial X_j^L}\right)dX_j^S+\sum_{j=2}^{n}\frac{\partial \Delta G_{DF}}{\partial X_j^S}dX_j^S$$
$$=\sum_{j=2}^{n}\sum_{k=2}^{n}\left(X_j^S-X_j^L\right)\frac{\partial^2 G_m^L}{\partial X_j^L\partial X_k^L}dX_k^L-\sum_{j=2}^{n}\frac{\partial \Delta G_{DF}}{\partial X_j^L}dX_j^L-\frac{\partial \Delta G_{DF}}{\partial v}dv \tag{15a}$$

$$\sum_{j=2}^{n}\frac{\partial^2 G_m^S}{\partial X_i^S\partial X_j^S}dX_j^S-\frac{\partial \Delta G_{D,m}^i}{\partial X_i^S}dX_i^S+\left(\frac{\partial^2 G_m^S}{\partial X_i^S\partial T}-\frac{\partial^2 G_m^L}{\partial X_i^L\partial T}-\frac{\partial \Delta G_{D,m}^i}{\partial T}\right)dT=\sum_{j=2}^{n}\frac{\partial^2 G_m^L}{\partial X_i^L\partial X_j^L}dX_j^L+\frac{\partial \Delta G_{D,m}^i}{\partial X_i^L}dX_i^L+\frac{\partial \Delta G_{D,m}^i}{\partial v}dv\ i\in(2,n) \tag{15b}$$

The relation of ΔG_D^j to interface velocity is not dependent on the drag parameter. Within the framework of chemical rate theory, Aziz has proposed the following formulation to relate the *trans*-interdiffusion (solute drag) driving force with the interface velocity for binary alloys:

$$\left(X_2^L-X_2^S\right)\frac{v}{v_D}=X_2^S\left(1-X_2^L\right)-\kappa_e X_2^L\left(1-X_2^S\right) \tag{13a}$$

$$\kappa_e\left(X_2^L,X_2^S,T\right)=\frac{X_1^LX_2^S}{X_1^SX_2^L}\exp\left(-\frac{\Delta G_D}{RT\left(X_2^L-X_2^S\right)}\right) \tag{13b}$$

where v_D is diffusive speed at interface. v_D is usually assumed to be scaled with the diffusivity in the liquid over an interatomic spacing; potentially v_D is obtainable from molecular dynamics calculations as it has been done in Ref. [30]. Also Smith and Aziz reported their experimental efforts in quantifying the values for v_D in various aluminum alloys [31], and their results will also be tested in our Results and discussions Section. It should be emphasized that the CALPHAD database includes thermodynamic interactions among the alloying elements, but the kinetic equations assume no interactions among alloying elements as the exchange terms among alloying term in Eq. (5) are ignored. It is acknowledged these terms may become important and will be considered for some multi-component alloys in our future study.

Thus, for binary alloys

$$\Delta G_D = -RT\left(X_2^L-X_2^S\right)\ln\left(1-\frac{\left(X_2^L-X_2^S\right)}{X_1^LX_2^S}\frac{v}{v_D}\right) \tag{13c}$$

For an n-ary alloy with the major component being component 1, κ_e^j, defined as partitioning parameter for component i, is related to ΔG_D^i

$$\left(X_i^L-X_i^S\right)\frac{v}{v_D^i}=X_i^S\left(1-X_i^L\right)-\kappa_e X_i^L\left(1-X_i^S\right) \tag{14a}$$

$$\kappa_e^i\left(X_i^L,X_i^S,T\right)=\frac{X_1^LX_i^S}{X_1^SX_i^L}\exp\left(-\frac{\Delta G_D^i}{RT\left(X_i^L-X_i^S\right)}\right) \tag{14b}$$

From Eqs. (14a) and (14b), the following equation can be derived for multi-component alloy:

$$\Delta G_D^i = -RT\left(X_i^L-X_i^S\right)\ln\left(1-\frac{\left(X_i^L-X_i^S\right)}{\left(1-X_i^L\right)X_i^S}\frac{v}{v_D^i}\right) \tag{14c}$$

2.3. Numerical solution of kinetic interface condition phase diagram

The kinetic interface condition phase diagram is *implicitly* defined by Eq. (9), Eq. (12) and Eq. (14c). To get the *explicit* relations describing the kinetic phase diagrams, the numerical integration method, proposed by the authors for phase boundary tracking and Gibbs-Thomson phase diagram calculation [28,29], is employed.

The first step to solve these equations is to get their differential forms, which are:

$\Delta G_{D,m}^i$ is defined as $\frac{\Delta G_D^i}{X_i^L-X_i^S}$ in the above equation. For the purpose of clarity, the independent variables being held constant in each partial derivative term of Eq. (15a) and Eq. (15b) are omitted. The partial derivatives of the liquid and solid phase molar Gibbs energies can be obtained from a CALPHAD database. In our implementation, TQ programing interface to Thermo-Calc™ software is used to get access to those derivatives. The partial derivatives of the driving energies with respect to temperature, composition and velocity can be derived from Eq. (12) and Eq. (14c), and they are listed in Appendix A.

Eq. (15) can be used to calculate the so-called interface sluggishness, i.e., the derivative of the kinetic liquidus with respect to interface velocity. Apply Eq. (15) to a binary system, and set $dX_j^L = 0$, one could get:

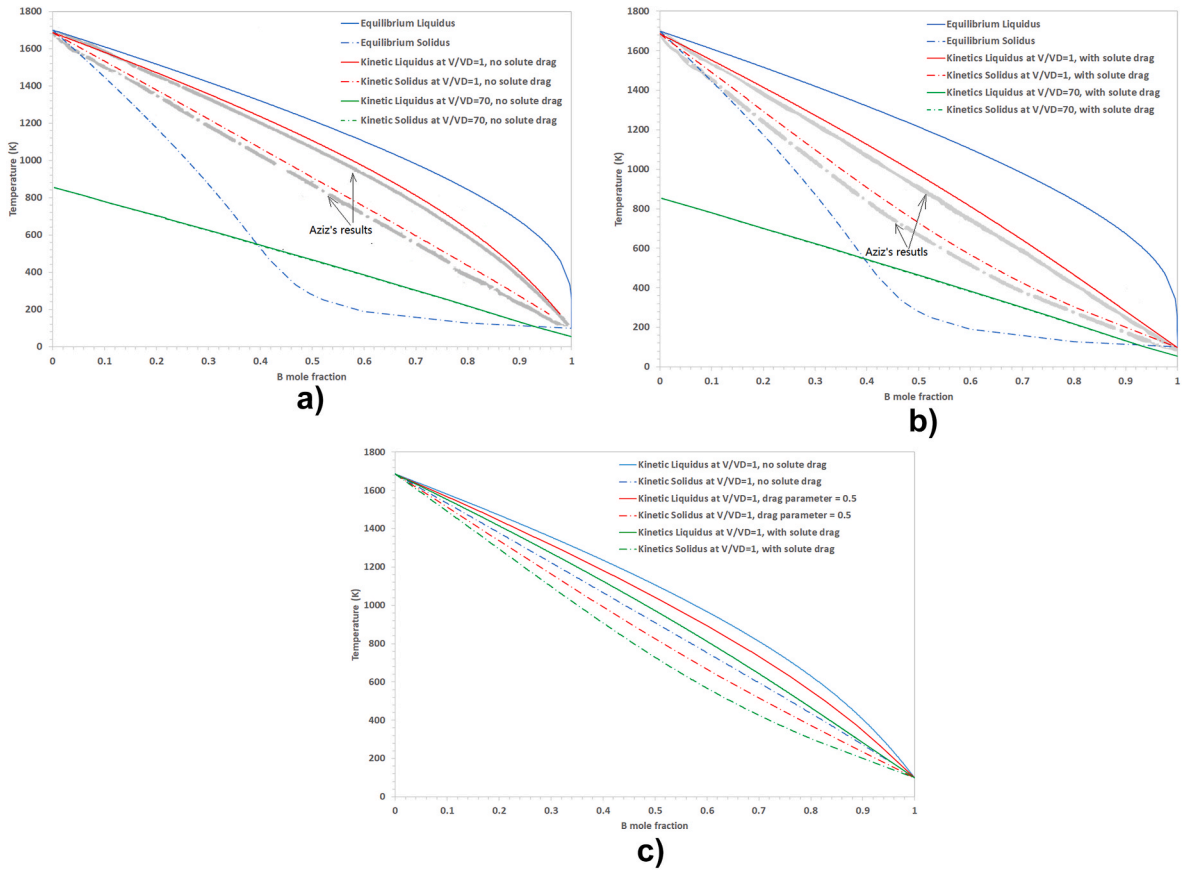

Fig. 1. Kinetic interface condition phase diagram for ideal solution liquid and solid at various v/v_D ratios; (a) no solute drag mode; (b) solute drag mode; (c) v/v_D = 1 with different drag modes. Solid line: kinetic liquidus. Dot-dashed line: kinetic solidus. Please note that the kinetic liquidus and solidus curves for v/v_D = 70 (the two green curves) in each figure are superposed on each other. The grey curves in Fig. 1a and b are reproduced from the curves (v/v_D = 1) of Fig. 4a and b of Reference [1].

$$\frac{\partial T}{\partial v}=\frac{\left(\frac{\partial G_m^S}{\partial X_2^S}-\frac{\partial G_m^L}{\partial X_2^L}+\frac{\partial \Delta G_{DF}}{\partial X_2^S}\right)\frac{\partial \Delta G_{D,m}^2}{\partial v}+\left(\frac{\partial^2 G_m^S}{\partial X_2^S \partial X_2^S}-\frac{\partial \Delta G_{D,m}^2}{\partial X_2^S}\right)\frac{\partial \Delta G_{DF}}{\partial v}}{\left(\frac{\partial G_m^S}{\partial X_2^S}-\frac{\partial G_m^L}{\partial X_2^L}+\frac{\partial \Delta G_{DF}}{\partial X_2^S}\right)\left(\frac{\partial^2 G_m^S}{\partial X_2^S \partial T}-\frac{\partial^2 G_m^L}{\partial X_2^L \partial T}-\frac{\partial \Delta G_{D,m}}{\partial T}\right)-\left(\frac{\partial^2 G_m^S}{\partial X_2^{S^2}}-\frac{\partial \Delta G_{D,m}}{\partial X_2^S}\right)\left(\frac{\partial G_m^S}{\partial T}-\frac{\partial G_m^L}{\partial T}+\frac{\partial \Delta G_{DF}}{\partial T}-\left(X_2^S-X_2^L\right)\frac{\partial^2 G_m^L}{\partial X_2^L \partial T}\right)} \tag{16}$$

Again for the purpose of clarity, the independent variables being held constant in each partial derivative term of Eq. (16) are omitted. Eq. (16) is a general form of Eq. A.15 in Aziz and Boettinger' article [17]. Applied to binary ideal solution phases and dilute limit assumption it would degenerate back to Eq. 2.23 in Ref. [17]. It is worthy noting that even Eq. (16) can not be analytically integrated, it gives some insights on the $T-v$ relation sought by Ludwig in Ref. [16] for multi-component alloys.

Eq. (15) is the key to our numerical solution of the CALPHAD-coupled multi-component continuous growth model. The equation relates the increments of temperature and X_i^S to any small increments of X_i^L and interface velocity. It is used to track the evolution of liquidus and solid phase composition with liquid phase composition/interface velocity. For illustrative purposes, the solution procedure for a domain bounded by the left bottom conner ($X_2^{L\,min}$,$X_3^{L\,min}$,$v^{min}=0$) and the right top conner ($X_2^{L\,max}$,$X_3^{L\,max}$,v^{max}) is described step by step as the following:

1. Start from the left bottom conner, where equilibrium (zero interface velocity) liquidus and solid phase compositions are known and set as the initial values for the following integration process. Set the integration direction along X_2^L as positive (toward the direction to $X_2^{L\,max}$).
2. Move at a small step along X_2^L from the current point while keeping X_3^L composition and velocity constant and calculate the increments of kinetic liquidus and solid phase composition according to Eq. (15). The integration methods such as Runge-Kutta method or the numerical continuation method described in Ref. [32] can be used here to achieve higher numerical efficiency.
3. Test if the right bound of $X_2^{L\,max}$ (or in the case with a negative integration direction, the left bound of $X_2^{L\,min}$) has been reached. If so, reverse the integration direction along X_2^L and go to Step 4, otherwise go to Step 2.
4. Test if the current X_3^L value is larger than $X_3^{L\,max}$. If so, go to step 5. Otherwise move at a small step along X_3^L while keep X_2^L and velocity constant and calculate the kinetic liquidus and solid phase composition according to Eq. (15), then go to step 2.
5. Test if the current value v is larger than v^{max}. If so, the whole domain has been swept, and the calculation stops. Otherwise move at a small

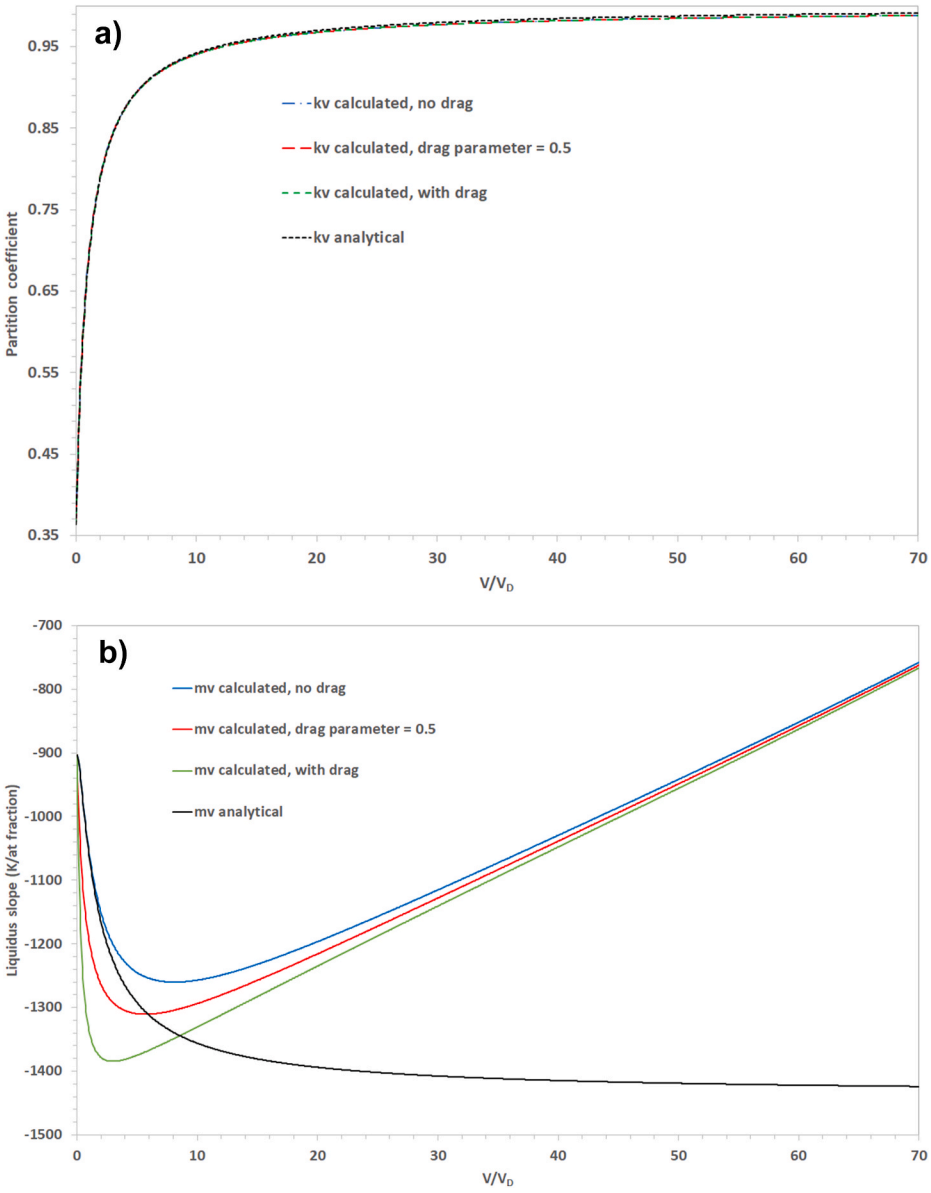

Fig. 2. The dependency of partition coefficient, (a), and liquidus slope, (b) on interface velocity under different drag modes for A- 6 at% B alloy. The analytical solution derived under no drag mode is also plotted.

step along v while keeping the liquid compositions (both X_2^I and X_3^I) constant and calculate the kinetic liquidus and solid phase composition according to Eq. (15), then go back to step 2.

One can refer to Ref. [28] for a graphical presentation of this integration-based numerical method when it was used for a similar numerical problem, i.e., the calculation of Gibbs-Thomson phase diagram.

3. Results and discussions

In this Section, the model behaviour is verified by its application to the hypothetical A-B ideal solution phases, Ag–Cu and Al–Be alloys. The model's practical values and ability of handling multi-component alloys are demonstrated by its applications to Al–Ti, Fe–Cr–Ni and Al–Cu–Mg–Si–Zn alloys. The application of the proposed model to additive manufacturing is demonstrated by calculating growth restriction factors from the predicted Al–Ti and Al–Cu–Mg–Si–Zn kinetic phase diagrams.

3.1. The application of ideal solid solution phases

The first application is to a hypothetical A-B system in which the liquid and solid are ideal solutions. For the purpose of model verification, all the materials parameters are set the same as the ones used in Ref. [1], i.e., the melting point for pure A and pure B are 1700 K and 100 K respectively, the molar entropy of fusion 10.1 J/(K•mol) and 9.0 J/(K•mol) respectively and $\frac{v_0}{v_D}$ is set as 100. Fig. 1 shows the kinetic liquidus and solidus calculated by our model under different drag modes together with equilibrium liquidus and solidus. The red curves, obtained at $\frac{v}{v_D} = 1$ under no drag mode in Fig. 1a, are in agreement with the grey curves obtained under the same conditions by Aziz et al. in Ref. [1]. The same observation can also be made for the red curves in Fig. 1b obtained at $\frac{v}{v_D} = 1$ with solute drag mode. It verifies our implementation of the reformulated continuous growth model. Fig. 1a and b also show, in green curves, the kinetic liquidus and solidus at $\frac{v}{v_D} = 70$. As expected, the liquidus and solidus curves drops well below their equilibrium counterparts and collapse together. Fig. 1c compares the kinetic liquidus and solidus obtained by different drag modes. The red curve of kinetic

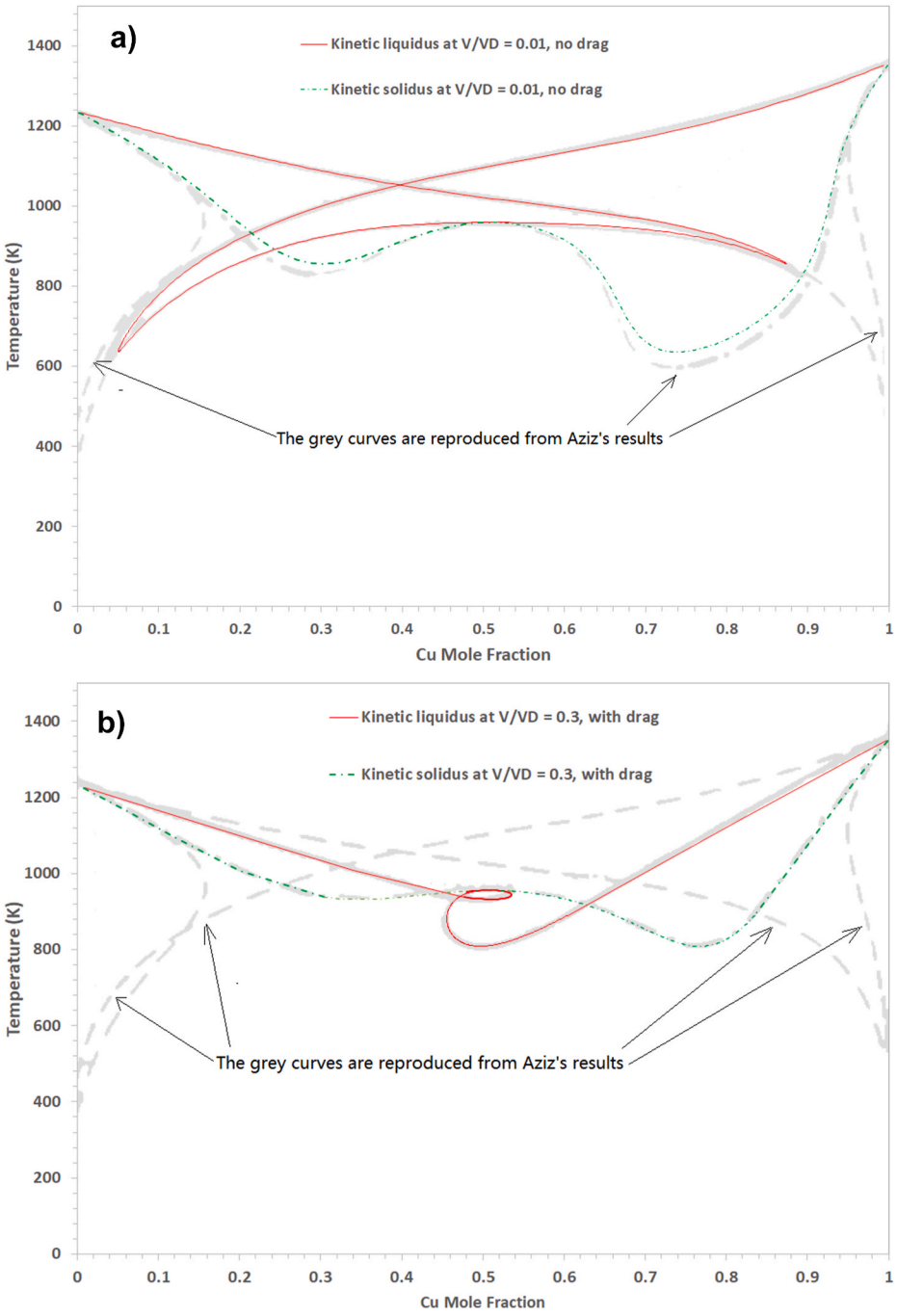

Fig. 3. Kinetic interface condition phase diagram for Ag–Cu alloys; (a) no solute drag mode at v/v_D = 0.01; (b) solute drag mode at v/v_D = 0.3; The grey lines in Fig. 3a and b are reproduced from the curves of Fig. 5a and Fig. 6b of Reference [1].

liquidus and solidus, obtained with the drag parameter of 0.5, lies in between their blue counterparts, which is obtained with the no-drag mode, and the green counterparts, which is obtained with the full drag mode. Fig. 1c reveals the important influences of drag parameters on the shape of kinetic phase diagram.

It is useful to compare the kinetic partition coefficient, k_v, and liquidus slope, m_v, calculated under different drag modes and by analytical solution [17]. Fig. 2 shows the results for A- 6 at% B alloy. Clearly the drag mode does not influence the dependency of k_v on interface velocity. It is due to that k_v is mostly determined by Eq. (14c), which has been used by all the three drag modes shown in Fig. 2a. The drag mode significantly influences the dependency of m_v on interface velocity when $\frac{v}{v_D}$ is less than 10, but the three modes tend to give the same m_v value when $\frac{v}{v_D}$ is larger than 15. The analytical solution to k_v and m_v with the no-drag mode, obtained under dilute ideal solution limit by Aziz et al. in Ref. [17], is presented in Fig. 2 with black solid lines. It is interesting to notice that the analytical solution to k_v is almost identical to the numerical solution, while the analytical m_v starts to deviate from the numerical solution when $\frac{v}{v_D}$ is large than 4. As the analytical solution was derived from the assumption of ideal solid solution phases, the discrepancy observed in Fig. 2b between the numerical and analytical results would be larger for the real alloys whose thermodynamics are often described by more complicated thermodynamic models including the contributions of sublattices and excess energies etc.

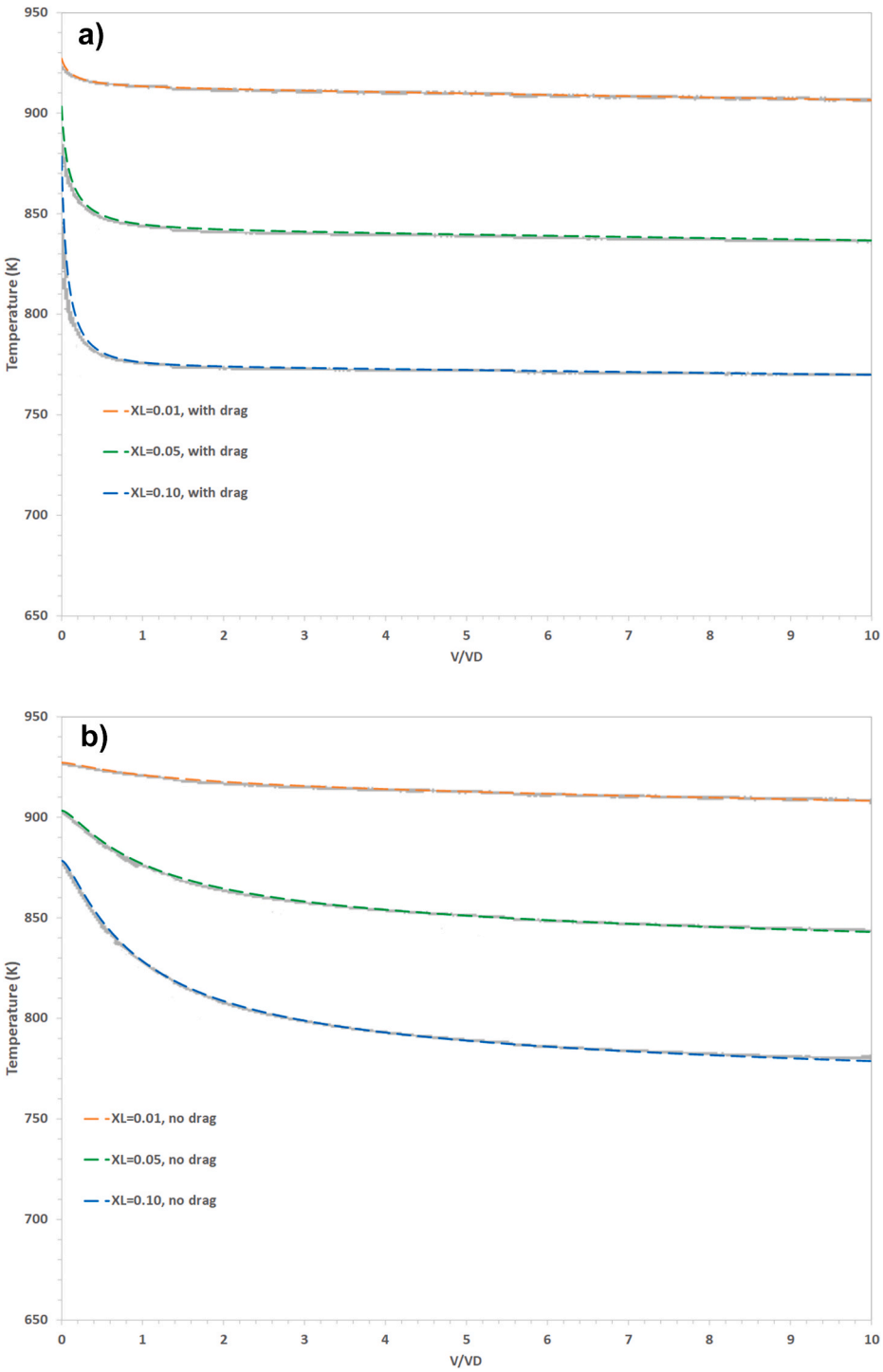

Fig. 4. The dependency of kinetic liquidus temperature on interface velocity obtained by the no-drag mode, (a), and solute drag mode, (b), at the liquid phase composition of Al-1at%Be, Al-5 at%Be and Al-10 at%Be. The grey lines in Fig. 4a and b are reproduced from the curves calculated by Aziz et al. with the same input parameters in Ref. [16].

3.2. Kinetic interface condition phase diagram of Ag–Cu, Al–Be and Al–Ti alloys

In this Section, the extended model is applied to various binary system with the purposes of model verification and behaviour demonstration. The first two applications are to Ag–Cu and Al–Be alloys, for which, kinetic phase diagrams have been calculated in Refs. [1,17]. The thermodynamic parameters in our calculations for these two alloys are set the same as the ones used in Refs. [1,17]. They are compiled into CALPHAD database files and provide as supplementary data to this paper. The thermodynamic parameters for Al–Ti are taken from commercial TTAL7 database. $\frac{v_0}{v_D}$ is set as 100 for Ag–Cu and 1000 for Al–Be as in Refs. [1,17], and $\frac{v_0}{v_D}$ is set as 100 for Al–Ti.

The red and green curves of Fig. 3a and Fig. 3b show the kinetic liquidus and solidus calculated under no drag mode at $\frac{v}{v_D} = 0.01$ and under drag mode at $\frac{v}{v_D} = 0.3$ respectively for Ag–Cu alloys. The grey dot-dashed curves in the background are the one obtained under the same conditions by Aziz et al. [1]. The grey dashed curves are the equilibrium

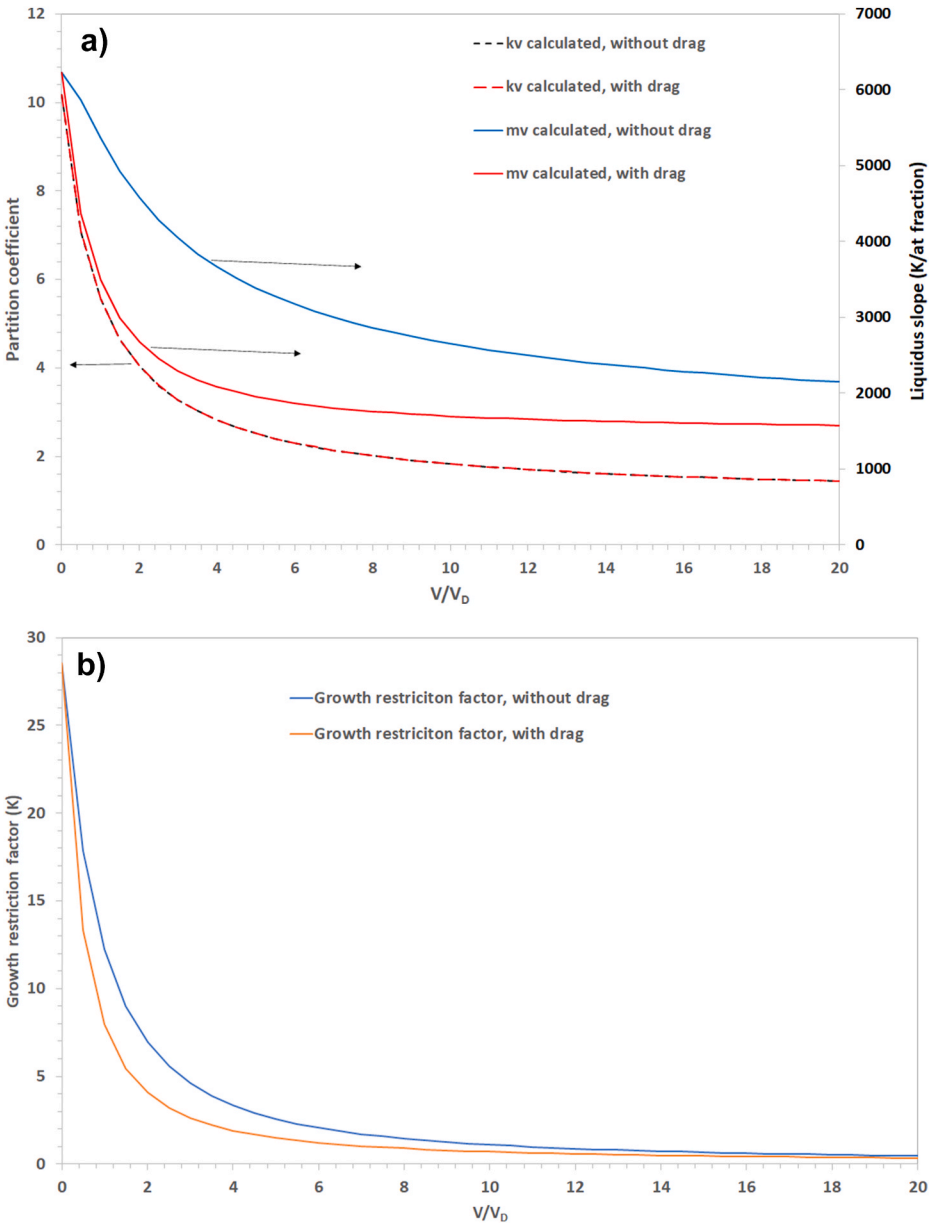

Fig. 5. The dependency of partition coefficient and liquidus slope, (a), and growth restriction factor, (b), on interface velocity under no drag and dray mode of Al-0.05 at%Ti alloy.

solidus and liquidus, and they are presented to highlight their significant differences from the kinetic ones. Clearly the complicate shapes of the kinetic solidus and liquidus are well reproduced by our proposed model, which servers as a strong verification of our model and its implementation.

The red, green and blues curves in Fig. 4 show the dependency of kinetic liquidus temperature on interface velocity for three liquid phase compositions: Al-1 at% Be, Al-5 at% Be and Al-10 at% Be respectively. Fig. 4a is the results obtained under no-drag mode, while Fig. 4b under solute drag mode. The grey curves in Fig. 4a and b are reproduced from the curves calculated by Aziz et al. with the same input parameters [17]. They are overlapping with the corresponding curves calculated by our model. This is the last case study to verify our model. The rest of case studies is to demonstrate its behaviour and practical values.

Fig. 5 is the simulation results obtained with CALPHAD database for Al-0.05 at% Ti alloy. It serves as the demonstration of the model behaviour for a technologically important alloy. In Fig. 5a the calculated kinetic partition coefficient, k_v, and liquidus slope, m_v, are plotted with discontinuous lines and solid lines, respectively. Clearly drag mode has little influence on kinetic coefficient, but significant influence on kinetic liquid slope. This observation echoes the ones with the ideal solid solution case study.

Fig. 5b plots growth restriction factor, Q, which is defined by the following equation:

$$Q = C_0 m(k-1) \tag{17}$$

Where C_0 is alloy composition, m liquid slope and k partition coefficient.

Growth restriction factor has been used successfully as an indicator for the effect of alloying component on grain refinement [33,34], and recently growth restriction factor has been discussed within the context of additive manufacturing [7,35]. Titanium is known as having a strong grain growth restrictor, and small amount of Ti solute to aluminum melt leads to significant grain size reduction in aluminum alloys under "normal" solidification conditions [36]. With the calculation of kinetic phase diagram, we now can calculate *kinetic growth restriction factor* to reveal how the effect of Ti on grain refinement under the condition of

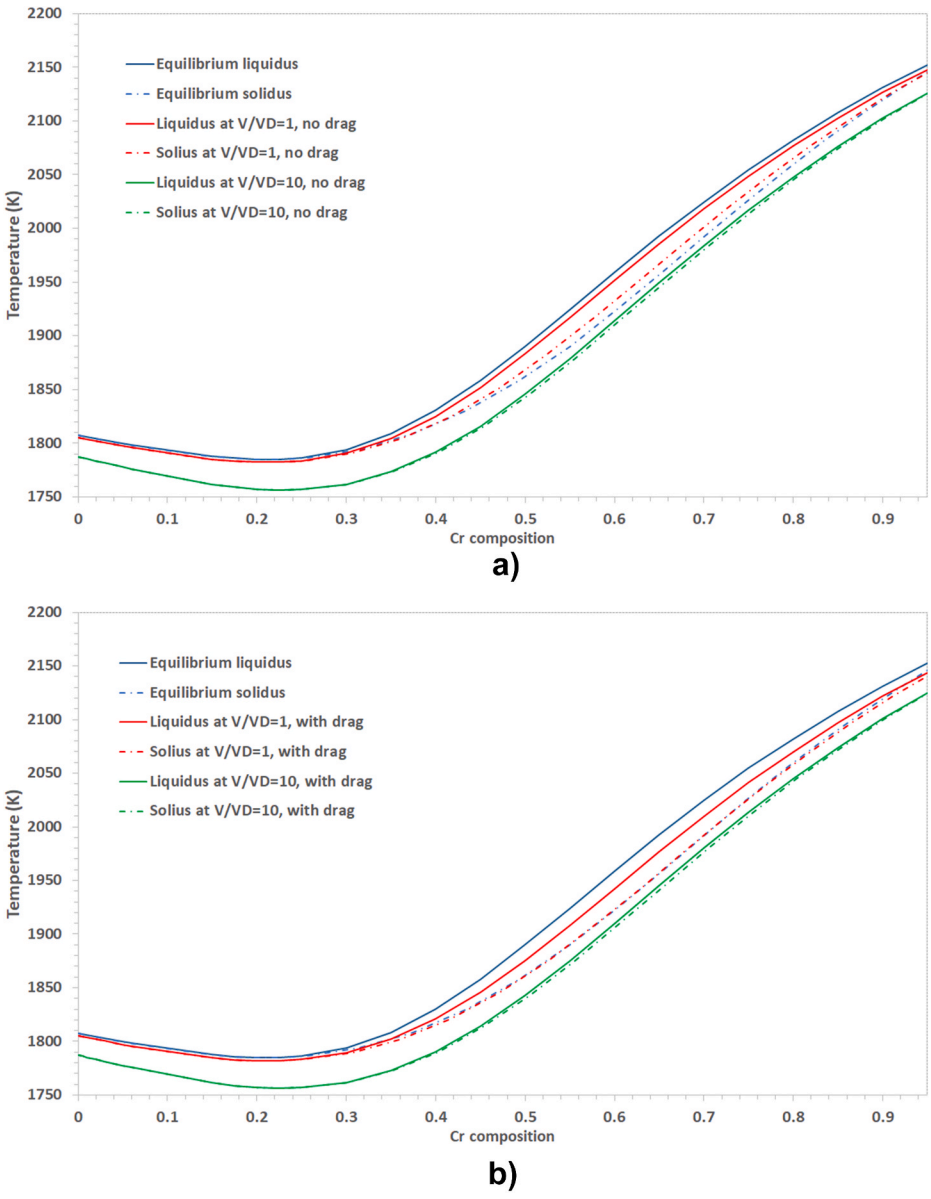

Fig. 6. The composition–temperature isopleth of an Fe–Cr–Ni kinetic interface condition phase diagram at various v/v_D ratios; the liquid phase Ni composition is fixed at 1 at% and Cr composition ranges from 0 at% to 95 at%; (a) no solute drag mode; (b) solute drag mode. Solid line: kinetic liquidus. Dot-dashed line: kinetic solidus.

the solid-liquid interface moving at different velocities. Fig. 5b present the dependence of growth restriction factor on interface velocity. Growth restriction factor, being very large at zero velocity, drop quickly with the increase of interface velocity. This decrease is due to both the approach of k to unity and the drop of liquidus slope as seen in Fig. 5a. Drag mode also influences this dependency with no drag mode having slightly less influences on growth restriction factor at the mediate range of interface velocity. Growth restriction factor approaches to zero when interface velocity is high as the result of kinetic partition coefficient being close to unity. This application demonstrates one of the practical values of kinetic phase diagram calculation, and in Section 3.4 kinetic growth restriction factors for a multi-component AM alloy will be calculated to shed light on the effects of each solute on grain refinement under AM solidification conditions.

3.3. Kinetic interface condition phase diagram of Fe–Cr–Ni alloys

In this section the multi-component model is applied to Fe–Cr–Ni alloys to demonstrate the model ability of handling complex shapes of multi-component kinetic phase diagrams. As shown in Fig. 6, the shape of equilibrium liquidus and solidus for this system is far from linear straight line, and therefore could provide stringent test to the model and its numerical solution method. The thermodynamic input parameters for this application are based on the ".tdb" file format CALPHAD database file provided in CALPHAD software PANDAT™ example book, and can be found in supplementary data of this paper. For this ternary alloy, there are two diffusive interface speed for the two alloying components, v_D^{Cr} and v_D^{Ni}, and these two input parameters are arbitrarily set the same as $\frac{v_0}{v_D^{Cr}} = \frac{v_0}{v_D^{Ni}} = \frac{v_0}{v_D} = 100$. Of course, when it comes to compare with experimentally measured kinetic phase diagrams, it is very important to know the dependency of diffusive interface speed on the temperature for each solute.

Fig. 6 plots the composition–temperature isopleths of an Fe–Cr–Ni kinetic interface condition phase diagram under two different drag modes. The liquid phase Ni composition is fixed at 1 at%, and Cr ranges from 0 to 95 at%. The kinetic liquidus and solidus at $\frac{v}{v_D} = 1$ and $\frac{v}{v_D} = 10$

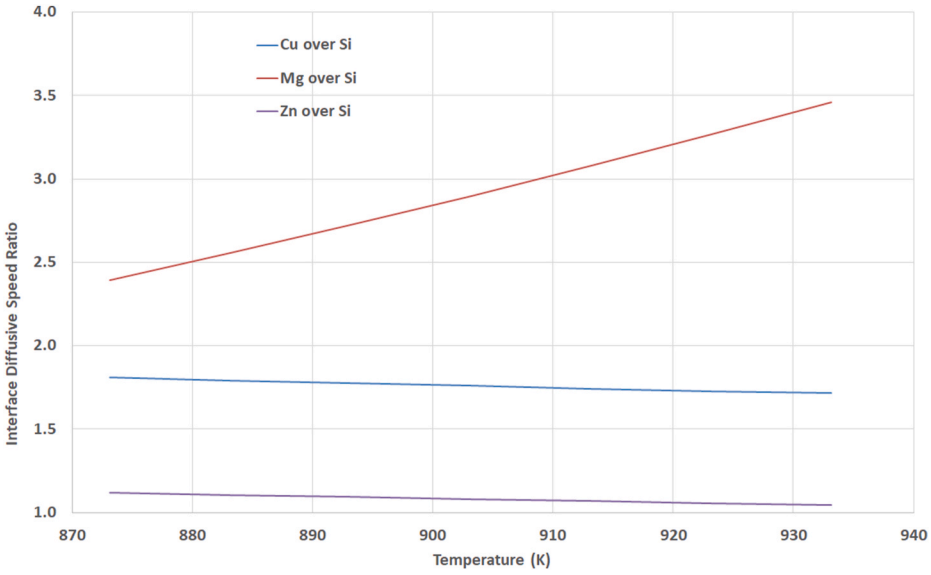

Fig. 7. The ratios of Cu, Mg and Zn diffusivities over Si diffusivity in liquid phase.

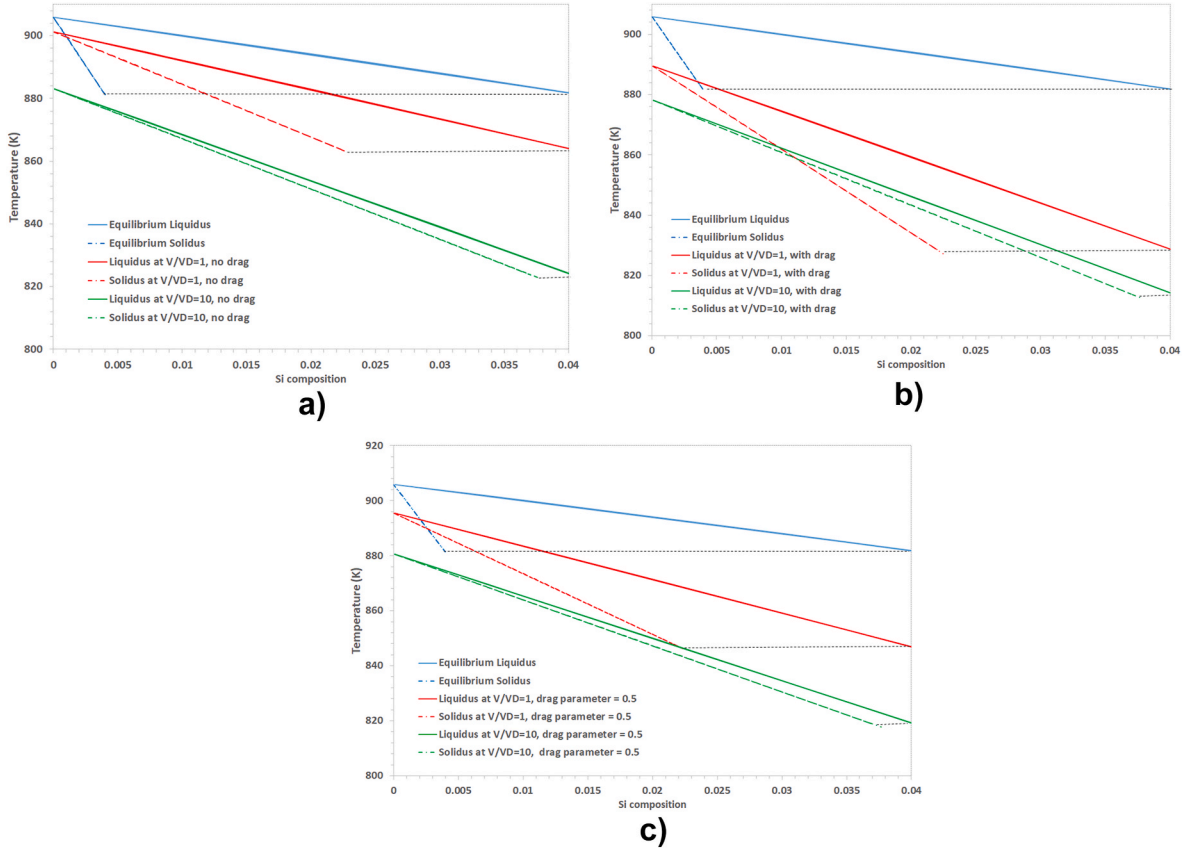

Fig. 8. The composition–temperature isopleth of an Al–Cu–Mg–Si–Zn kinetic interface condition phase diagram at various v/v_D ratios; the Cu, Mg, Zn compositions in liquid phase are fixed at 0.73 at% (2.8 wt%),2.88 at% (2.48 wt%), 2.81 at% (6.52 wt%) respectively while Si ranges from 0 at% to 4.1 at% (4 wt%); (a) no solute drag mode; (b) solute drag mode; (c) mixed mode drag with the drag parameter set to 0.5. Solid line: kinetic liquidus. Dot-dashed line: kinetic solidus.

are presented together with the equilibrium liquidus and solidus (blue curves) in Fig. 6a and b. At $\frac{v}{v_D} = 1$ for Cr composition less than 30 at% the kinetic liquidus and solidus (the red curves in Fig. 6a and b) exhibit little deviation from their equilibrium counterparts. The deviation becomes more and more noticeable when Cr composition is higher 30 at%. The kinetic liquidus and solidus are closer than their equilibrium counterparts are. Drag mode certainly influences how kinetic liquids and solidus change. By contrasting Fig. 6a and b, one can see that the kinetic liquidus deviates more from the equilibrium liquidus under drag mode than no-drag mode. At $\frac{v}{v_D} = 10$, the kinetic liquidus drops more than 25K below the equilibrium liquidus, and it also collapses into the kinetic solidus. At this high interface velocity, drag mode has insignificant

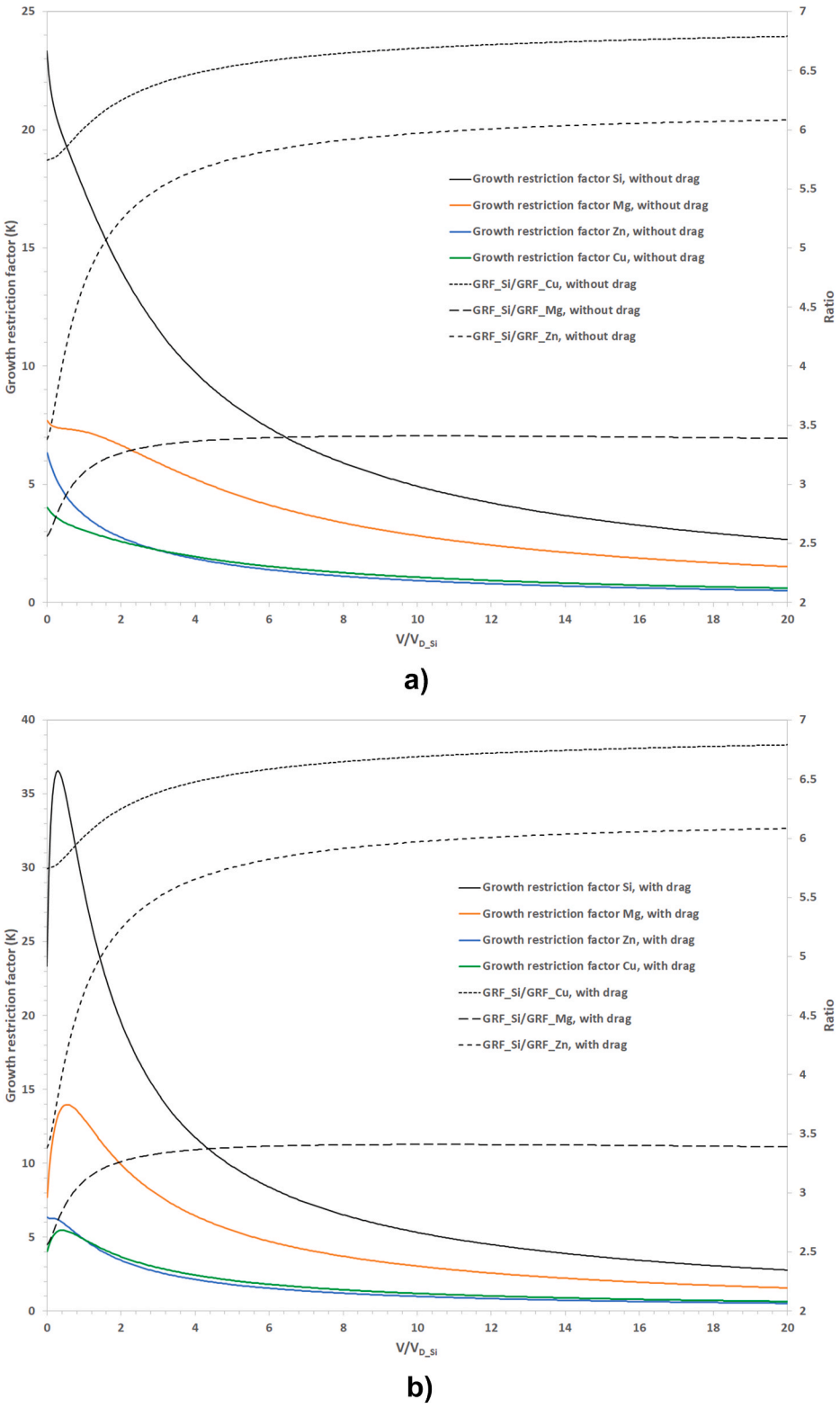

Fig. 9. The dependency of growth restriction factor on interface velocity under no drag mode, (a), and drag mode, (b), of an Al-0.73 at%Cu-2.88 at%Mg-4.1 at%Si-2.81 at%-Zn alloy. The ratios of Cu, Mg and Zn interface diffusive speeds over Si speed is calculated according to these elements diffusivities values in liquid phase.

influences on the shape of the kinetic liquidus and solidus.

3.4. Kinetic interface condition phase diagram of Al–Cu–Mg–Si–Zn alloys and growth restriction factor

The application to Al–Cu–Mg–Si–Zn quinary alloy system is presented in this section. This purpose of this application is two-folded. It is not only to demonstrate the model's ability to handle multi-component alloys, but also one of the practical values of multi-component kinetic phase diagram calculation. It has been observed recently from additive manufacturing experiments that adding Si can improve the printability of Al–Cu–Mg–Zn (AA7075) alloys [37,38]. One

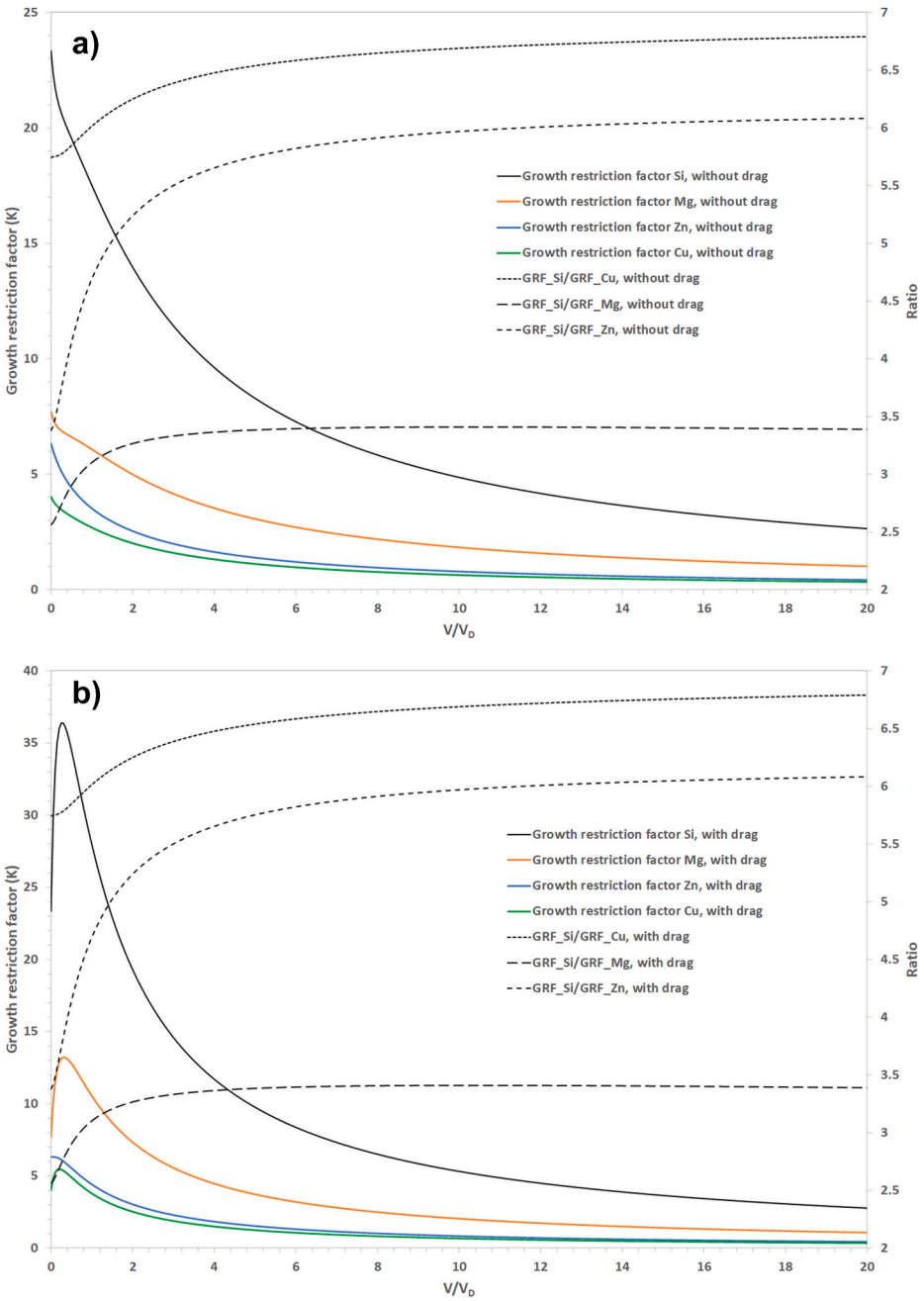

Fig. 10. The dependency of growth restriction factor on interface velocity under no drag mode, (a), and drag mode, (b), of an Al-0.73 at%Cu-2.88 at%Mg-4.1 at%Si-2.81 at%-Zn alloy. The interface diffusive speeds for the four alloying components are set artificially as identical.

hypothesis to explain this improvement caused by Si modification is its grain refinement effect [37,38]. The proposed model can calculate kinetic growth restriction factor as demonstrated in Fig. 5, and it will be applied here to evaluate Si effect on grain refinement under the fast-cooling condition encountered during AM.

The thermodynamic input parameters for this application are taken from TTAL7 CALPHAD database. For this quinary alloy, there are four diffusive interface speed for the four alloying components, v_D^{Cu}, v_D^{Mg}, v_D^{Si} and v_D^{Zn}. The value of diffusive interface speed, as mentioned Section 2.2, can be calculated from interface diffusivities and interatomic spacing in Ref. [17], i.e., for solute j,

$$v_D^j = \frac{\overline{D}_j}{\lambda} \tag{18}$$

Where $\overline{D}_j$ is the diffusivity inside the interface of element j, and λ is interatomic spacing. In principle, $\overline{D}_j$ and λ are obtainable from first principle and molecular dynamics calculations. However, such a calculation for the four alloying components is not included in this manuscript, and will be included in our future work. Instead following the approach adopted by Aziz and Boettiger in Ref. [17], the magnitude of $\overline{D}_j$ are estimated from the diffusivity in the parent (liquid) phase. With the liquid diffusivities data provided in Ref. [39], the ratios of the interface diffusive speed of Cu, Mg and Zn over the one of Si are plotted in Fig. 7. Among the three alloying components, Cu diffuses the fastest while Zn has the similar diffusivity as Si. Mg's diffusivity is about 1.5 times the one of Si. The other input parameter, v_0, is set to be $100v_D^{Si}$.

Fig. 8 plots the composition–temperature isopleths of an Al–Cu–Mg–Si–Zn kinetic interface condition phase diagram under three

different drag modes. The liquid phase Cu, Mg, Zn compositions are fixed at 0.73 at% (2.8 wt%),2.88 at% (2.48 wt%), 2.81 at% (6.52 wt%) respectively while Si ranges from 0 at% to 4.1 at% (4 wt%). These range covers the experimental composition matrix reported in Ref. [38]. The kinetic liquidus and solidus at $\frac{v}{v_D^{Si}} = 1$ and $\frac{v}{v_D^{Si}} = 100$ are presented together with the equilibrium liquidus and solidus in Fig. 8a, b and c. At $\frac{v}{v_D^{Si}} = 1$ the kinetic liquidus slope becomes steeper, and the liquidus and solidus are closer than their equilibrium counterparts are. Drag mode certainly influences the extent at which liquids slope change, and no-drag mode has the least influence. At $\frac{v}{v_D^{Si}} = 100$, the kinetic liquidus drops more than 50 K below the equilibrium liquidus, and it collapses into the kinetic solidus. At this high interface velocity, drag mode has an insignificant influence on the shape of the kinetic liquidus and solidus.

Fig. 9a and b show, with solid lines, the dependency of growth restriction factor of all the four alloying components (Si, Mg, Zn and Cu) on interface velocity under no-drag mode and drag mode, respectively. To highlight the relative weight of Si to other alloying components, the ratio of Si growth restriction factor over the other three components also are plotted in Fig. 9 with discontinuous curves. Si growth restriction factor is 23.5 K at zero interface velocity, which is 5.7, 2.6 and 3.4 times the growth restriction factor of Cu, Mg and Si as seen from the discontinuous curves from Fig. 9a and b. Si effect on grain refinement under "non-rapid" condition is significant evidenced by its large growth restriction factor value. Under no-drag mode, although growth restriction factor of all the solutes decreases, the ratio of Si over the other solutes increases, indicating that Si becomes even more important than all the other components for grain refinement under rapid or sub-rapid solidification conditions. Under solute drag mode, growth restriction factors of all the solutes exhibit a quick increase before dropping with the increase of interface velocity. Again, the ratios of Si over the other solutes increase with the increase of interface velocity highlighting the important role of Si for grain refinement. The calculated growth restriction factors curves are in consistency with the experimental observation of the pronounced effect of Si on grain refinement during additive manufacturing [37,38].

It should be mentioned that the approximation made with this analysis here is the diffusive interface speeds, v_D^{Cu}, v_D^{Mg}, v_D^{Si} and v_D^{Zn} are estimated from the diffusivities in the liquid phase. To test the sensitivity of the calculation results on these parameters vales, a simulation with constant and identical interface diffusive speed for all alloying components is performed. With these new input parameters, the predicted GRF curves of Mg and Cu, shown in Fig. 10, deviate from their corresponding ones in Fig. 9; noticeably the curve of GRF Cu cross the one of GRF Zn in Fig. 9 while no such cross is observed in Fig. 10. The values of relative interface speed at which Cu and Mg GRF curves attains their maximum values are different from their corresponding ones in Fig. 9, and they are shifted leftwards. The predicted GRF curves of Zn and Si in Fig. 10 are very close to their corresponding ones in Fig. 9. However, clearly the trend observed in Fig. 9 does not change, i.e., with the increase of interface velocity, the ratio of Si growth restriction factor over the other solutes increases. Si is still predicted to be the more important than all the other components for grain refinement under rapid or sub-rapid solidification conditions.

We also run the simulations with the diffusive interface speeds, v_D^{Cu}, v_D^{Mg}, v_D^{Si} and v_D^{Zn} calculated by the empirical formula proposed by Smith and Aziz for various aluminum alloys in Ref. [31]. The formula can be approximated written as in the following form:

$$v_D \propto k^{-0.6} \tag{19}$$

With a constant partition coefficient for each solute, estimated from our CALPHAD database, i.e. 0.14 for Cu, 0.3 for Mg, 0.11 for Si and 0.41 for Zn, the calculated ratios are 0.86, 0.54 and 0.45 respectively. A new simulation with these ratios is performed, and its results still verify the profound effects of Si. For clarity reasons, the results are not included.

The sensitivity study of the calculation results on v_0 value also have been conducted. Simulations with $\frac{v_0}{v_D^{Si}}$ ratio of 50, 150 and 1000 are performed, and it is confirmed that the said Si effect is presented in all these simulations. For clarity reasons, the calculated GRF curves are not presented here.

4. Summary and conclusions

In this paper we have reformulated the binary continuous growth models into a form suitable for the coupling with the CALPHAD databases of multi-component alloy systems. A numerical solution to the CALPHAD-coupled multi-component model is described. The model and its numerical solution are verified by the case studies with ideal solution phases, Ag–Cu and Al–Be alloy. The model predictive power and practical values are demonstrated by the case studies with Al–Ti, Fe–Cr–Ni and Al–Cu–Mg–Si–Zn alloys. It is expected that the proposed framework is applicable to solid state phase transformation in which the linear kinetic laws prevail. The interface-velocity dependent partition coefficient and liquid slope calculated in this paper is ready to be integrated into a columnar equiaxed transition model to predict grain morphology formed under directional rapid solidification condition.

The work raises some research questions to be addressed in the future. One interesting one is to explore how the drag parameter, β, depends on interface velocity and the diffusion in the bulk. As proposed in Ref. [20], there is a major difference between the behavior of the interface at low and high velocities, and the multi-component model can be extended to incorporate a velocity-dependent drag parameter. The second one is whether the kinetic interface phase diagram calculation is equivalent to the minimization of some forms of Gibbs energy function. There have been some research activities relating the calculation of interfacial interface conditions with thermodynamic extremum principle [40–43], and it is worth exploring how to use the extremum principle when the kinetic law is not linear but exponential as in the continuous growth model. The third one is computational study of the kinetic input parameters to the proposed model such as interface diffusive speed. Such a study would enable accurate calculation of kinetic phase diagram with the proposed model, thus release the great potential of thermodynamic database for AM alloy design and processing parameter optimization.

Declaration of competing interest

The authors declare that they have no known competing financial interests or personal relationships that could have appeared to influence the work reported in this paper.

Acknowledgement

This research work is funded by Norsk Hydro's Fond under the grant name "A Framework for the Development of Printable Al Alloys for Powder Bed Additive Manufacturing" and by the SFI PhysMet "Center for sustainable and competitive metallurgical and manufacturing industry" with support from the Research Council of Norway and the industrial partners under the grant number of 309584/F40.

Appendix A. Supplementary data

Supplementary data to this article can be found online at https://doi.org/10.1016/j.calphad.2021.102365.

Appendix

Appendix A. the derivatives of driving energies

From Eq. (12), the partial derivatives of the overall molar driving energy ΔG_{DF} can be written bellow:

$$\left(\frac{\partial \Delta G_{DF}}{\partial T}\right)_{X_i^S, X_j^L, v} = -R\ln\left(1-\frac{v}{v_0}\right) + \beta\sum_{k=2}^{n}\left(\frac{\partial \Delta G_D^k}{\partial T}\right)_{X_i^S, X_j^L, v} \tag{A.1a}$$

$$\left(\frac{\partial \Delta G_{DF}}{\partial X_j^S}\right)_{T, X_i^S, X_k^L, v} = \beta\left(\frac{\partial \Delta G_D^j}{\partial X_j^S}\right)_{T, X_i^S, X_k^L, v} \tag{A.1b}$$

$$\left(\frac{\partial \Delta G_{DF}}{\partial X_j^L}\right)_{T, X_i^S, X_k^L, v} = \beta\left(\frac{\partial \Delta G_D^j}{\partial X_j^L}\right)_{T, X_i^S, X_k^L, v} \tag{A.1c}$$

$$\left(\frac{\partial \Delta G_{DF}}{\partial v}\right)_{T, X_i^S, X_k^L} = \frac{RT}{v_0 - v} + \beta\sum_{j=2}^{n}\left(\frac{\partial \Delta G_D^j}{\partial v}\right)_{T, X_i^S, X_k^L} \tag{A.1d}$$

Before calculating the derivatives of Eq. (14c), the following definition is made:

$$\Delta G_{D,m}^i \equiv \frac{\Delta G_D^i}{X_i^L - X_i^S} = -RT\ln\left(1-\frac{\left(X_i^L - X_i^S\right)}{\left(1-X_i^L\right)X_i^S}\frac{v}{v_D^i}\right) \tag{A.2}$$

The derivatives of the molar driving force, $\Delta G_{D,m}^i$ is listed below:

$$\left(\frac{\partial \Delta G_{D,m}^i}{\partial T}\right)_{X_i^S, X_j^L, v} = -R\ln\left(1-\frac{\left(X_i^L - X_i^S\right)}{\left(1-X_i^L\right)X_i^S}\frac{v}{v_D^i}\right) \tag{A3.1}$$

$$\left(\frac{\partial \Delta G_{D,m}^i}{\partial X_i^L}\right)_{T, X_j^S, X_k^L, v} = \frac{RT}{1-\frac{\left(X_i^L - X_i^S\right)}{\left(1-X_i^L\right)X_i^S}\frac{v}{v_D^i}}\frac{v}{v_D^i}\left(\frac{1-X_i^S}{\left(1-X_i^L\right)^2 X_i^S}\right) \tag{A3.2}$$

$$\left(\frac{\partial \Delta G_{D,m}^i}{\partial X_i^S}\right)_{T, X_j^S, X_k^L, v} = -\frac{RT}{1-\frac{\left(X_i^L - X_i^S\right)}{\left(1-X_i^L\right)X_i^S}\frac{v}{v_D^i}}\frac{v}{v_D^i}\frac{X_i^L}{X_i^{S2}\left(1-X_i^L\right)} \tag{A3.3}$$

$$\left(\frac{\partial \Delta G_{D,m}^i}{\partial v}\right)_{T, X_i^S, X_k^L} = \frac{RT}{1-\frac{\left(X_i^L - X_i^S\right)}{\left(1-X_i^L\right)X_i^S}\frac{v}{v_D^i}}\frac{\left(X_i^L - X_i^S\right)}{\left(1-X_i^L\right)X_i^S}\frac{1}{v_D^i} \tag{A3.4}$$

Therefore, the derivatives of the solute redistribution driving energy can be written below:

$$\left(\frac{\partial \Delta G_D^j}{\partial T}\right)_{X_i^S, X_j^L, v} = \left(X_i^L - X_i^S\right)\left(\frac{\partial \Delta G_{D,m}^i}{\partial T}\right)_{X_i^S, X_j^L, v} \tag{A4.1}$$

$$\left(\frac{\partial \Delta G_D^j}{\partial X_j^S}\right)_{T, X_i^S, X_k^L, v} = -\Delta G_{D,m}^i + \left(X_i^L - X_i^S\right)\left(\frac{\partial \Delta G_{D,m}^j}{\partial X_j^S}\right)_{T, X_i^S, X_k^L, v} \tag{A4.2}$$

$$\left(\frac{\partial \Delta G_D^j}{\partial X_j^L}\right)_{T, X_i^S, X_k^L, v} = \Delta G_{D,m}^i + \left(X_i^L - X_i^S\right)\left(\frac{\partial \Delta G_{D,m}^j}{\partial X_j^L}\right)_{T, X_i^S, X_k^L, v} \tag{A4.3}$$

$$\left(\frac{\partial \Delta G_D^j}{\partial v}\right)_{T, X_i^S, X_k^L} = \left(X_i^L - X_i^S\right)\left(\frac{\partial \Delta G_D^j}{\partial v}\right)_{T, X_i^S, X_k^L} \tag{A4.4}$$

Note that these derivatives are derived with the simplification that v_0 and v_D^i are constant. It is straightforward to calculate the derivatives when they are dependent on temperature or composition.

References

[1] M.J. Aziz, T. Kaplan, Continuous growth model for interface motion during alloy solidification, Acta Metall. 36 (8) (1988) 2335–2347.

[2] J.C. Baker, J.W. Cahn, Thermodynamics of Solidification, The Selected Works of John W. Cahn, 1998, pp. 253–288.

[3] M. Hillert, Solute drag, solute trapping and diffusional dissipation of Gibbs energy11This paper is based on the Hume–Rothery Lecture presented at the 128th

TMS Annual Meeting, 1 March 1999, San Diego, U.S.A, Acta Mater. 47 (18) (1999) 4481–4505.
[4] N.T. Aboulkhair, M. Simonelli, L. Parry, I. Ashcroft, C. Tuck, R. Hague, 3D printing of Aluminium alloys: Additive Manufacturing of Aluminium alloys using selective laser melting, Prog. Mater. Sci. 106 (2019).
[5] M.J. Bermingham, D.H. StJohn, J. Krynen, S. Tedman-Jones, M.S. Dargusch, Promoting the columnar to equiaxed transition and grain refinement of titanium alloys during additive manufacturing, Acta Mater. 168 (2019) 261–274.
[6] P. Mohammadpour, A. Plotkowski, A.B. Phillion, Revisiting solidification microstructure selection maps in the frame of additive manufacturing, Addit. Manuf. 31 (2020).
[7] J.H. Martin, B. Yahata, J. Mayer, R. Mone, E. Stonkevitch, J. Miller, M.R. O'Masta, T. Schaedler, J. Hundley, P. Callahan, T. Pollock, Grain refinement mechanisms in additively manufactured nano-functionalized aluminum, Acta Mater. 200 (2020) 1022–1037.
[8] H. Hyer, L. Zhou, A. Mehta, S. Park, T. Huynh, S. Song, Y. Bai, K. Cho, B. McWilliams, Y. Sohn, Composition-dependent solidification cracking of aluminum-silicon alloys during laser powder bed fusion, Acta Mater. 208 (2021).
[9] J. Ågren, A simplified treatment of the transition from diffusion controlled to diffusion-less growth, Acta Metall. 37 (1) (1989) 181–189.
[10] L. Zi-Kui, J. Ågren, On the transition from local equilibrium to paraequilibrium during the growth of ferrite in Fe-Mn-C austenite, Acta Metall. 37 (12) (1989) 3157–3163.
[11] H. Wang, F. Liu, G.J. Ehlen, D.M. Herlach, Application of the maximal entropy production principle to rapid solidification: A multi-phase-field model, Acta Mater. 61 (7) (2013) 2617–2627.
[12] X. Yang, L. Zhang, S. Sobolev, Y. Du, Kinetic Phase Diagrams of Ternary Al-Cu-Li System during Rapid Solidification: A Phase-Field Study, Materials 11 (2) (2018).
[13] T. Keller, G. Lindwall, S. Ghosh, L. Ma, B.M. Lane, F. Zhang, U.R. Kattner, E.A. Lass, J.C. Heigel, Y. Idell, M.E. Williams, A.J. Allen, J.E. Guyer, L.E. Levine, Application of Finite Element, Phase-field, and CALPHAD-based Methods to Additive Manufacturing of Ni-based Superalloys, Acta Mater. 139 (2017) 244–253.
[14] T. Pinomaa, N. Provatas, Quantitative phase field modeling of solute trapping and continuous growth kinetics in quasi-rapid solidification, Acta Mater. 168 (2019) 167–177.
[15] S. Kavousi, M. Asle Zaeem, Quantitative phase-field modeling of solute trapping in rapid solidification, Acta Mater. 205 (2021).
[16] A. Ludwig, The interface response-functions in multi-componental alloy solidification, Phys. Nonlinear Phenom. 124 (1) (1998) 271–284.
[17] M.J. Aziz, W.J. Boettinger, On the transition from short-range diffusion-limited to collision-limited growth in alloy solidification, Acta Metall. Mater. 42 (2) (1994) 527–537.
[18] J.A. Kittl, M.J. Aziz, D.P. Brunco, M.O. Thompson, Absence of solute drag in solidification, Appl. Phys. Lett. 64 (18) (1994) 2359–2361.
[19] J.A. Kittl, P.G. Sanders, M.J. Aziz, D.P. Brunco, M.O. Thompson, Complete experimental test of kinetic models for rapid alloy solidification, Acta Mater. 48 (20) (2000) 4797–4811.
[20] M.E. Gurtin, P.W. Voorhees, The thermodynamics of evolving interfaces far from equilibrium, Acta Mater. 44 (1) (1996) 235–247.
[21] K. Wang, H. Wang, F. Liu, H. Zhai, Modeling rapid solidification of multi-component concentrated alloys, Acta Mater. 61 (4) (2013) 1359–1372.
[22] J. Draxler, J. Edberg, J. Andersson, L.E. Lindgren, Modeling and simulation of weld solidification cracking part II, Weld. World 63 (5) (2019) 1503–1519.
[23] S.J. Foster, K. Carver, R.B. Dinwiddie, F. List, K.A. Unocic, A. Chaudhary, S.S. Babu, Process-Defect-Structure-Property Correlations During Laser Powder Bed Fusion of Alloy 718: Role of In Situ and Ex Situ Characterizations, Metall. Mater. Trans. 49 (11) (2018) 5775–5798.
[24] A. Jacot, M. Rappaz, A pseudo-front tracking technique for the modelling of solidification microstructures in multi-component alloys, Acta Mater. 50 (8) (2002) 1909–1926.
[25] Q. Du, A. Jacot, A two-dimensional micro segregation model for the description of microstructure formation during solidification in multicomponent alloys: Formulation and behaviour of the model, Acta Mater. 53 (12) (2005) 3479–3493.
[26] I. Steinbach, Phase-field models in materials science, Model. Simulat. Mater. Sci. Eng. 17 (7) (2009), 073001.
[27] P. Galenko, Extended thermodynamical analysis of a motion of the solid-liquid interface in a rapidly solidifying alloy, Phys. Rev. B 65 (14) (2002).
[28] Q. Du, M. Perez, W.J. Poole, M. Wells, Numerical integration of the Gibbs-Thomson equation for multicomponent systems, Scripta Mater. 66 (7) (2012) 419–422.
[29] Q. Du, M.A. Wells, Tracking multi-phase boundaries using an integration-based approach, Comput. Mater. Sci. 50 (11) (2011) 3153–3161.
[30] P. Geysermans, D. Gorse, V. Pontikis, Molecular dynamics study of the solid–liquid interface, J. Chem. Phys. 113 (15) (2000) 6382–6389.
[31] P.M. Smith, M.J. Aziz, Solute trapping in aluminum alloys, Acta Metall. Mater. 42 (10) (1994) 3515–3525.
[32] E.L.A.G. Allgower, Kurt, Introduction to Numerical Continuation Methods.
[33] Z. Fan, F. Gao, L. Zhou, S.Z. Lu, A new concept for growth restriction during solidification, Acta Mater. 152 (2018) 248–257.
[34] R. Schmid-Fetzer, A. Kozlov, Thermodynamic aspects of grain growth restriction in multicomponent alloy solidification, Acta Mater. 59 (15) (2011) 6133–6144.
[35] A. Prasad, L. Yuan, P. Lee, M. Patel, D. Qiu, M. Easton, D. StJohn, Towards understanding grain nucleation under Additive Manufacturing solidification conditions, Acta Mater. 195 (2020) 392–403.
[36] Q. Du, Y. Li, An extension of the Kampmann–Wagner numerical model towards as-cast grain size prediction of multicomponent aluminum alloys, Acta Mater. 71 (2014) 380–389, 0.
[37] G. Li, S.D. Jadhav, A. Martín, M.L. Montero-Sistiaga, J. Soete, M.S. Sebastian, C. M. Cepeda-Jiménez, K. Vanmeensel, Investigation of Solidification and Precipitation Behavior of Si-Modified 7075 Aluminum Alloy Fabricated by Laser-Based Powder Bed Fusion, Metall. Mater. Trans. 52 (1) (2020) 194–210.
[38] M.L. Montero-Sistiaga, R. Mertens, B. Vrancken, X. Wang, B. Van Hooreweder, J.-P. Kruth, J. Van Humbeeck, Changing the alloy composition of Al7075 for better processability by selective laser melting, J. Mater. Process. Technol. 238 (2016) 437–445.
[39] Y. Du, Y.A. Chang, B.Y. Huang, W.P. Gong, Z.P. Jin, H.H. Xu, Z.H. Yuan, Y. Liu, Y. H. He, F.Y. Xie, Diffusion coefficients of some solutes in fcc and liquid Al: critical evaluation and correlation, Mater. Sci. Eng. A-Struct. Mater. Properties Microstruct. Process. 363 (1–2) (2003) 140–151.
[40] E. Gamsjäger, A concise derivation of the contact conditions at a migrating sharp interface, Phil. Mag. Lett. 88 (5) (2008) 363–369.
[41] M. Hillert, J. Agren, Extremum principles for irreversible processes, Acta Mater. 54 (8) (2006) 2063–2066.
[42] F.D. Fischer, J. Svoboda, H. Petryk, Thermodynamic extremal principles for irreversible processes in materials science, Acta Mater. 67 (2014) 1–20, 0.
[43] W.C. Carter, J.E. Taylor, J.W. Cahn, Variational methods for microstructural-evolution theories, JOM (J. Occup. Med.) 49 (12) (1997) 30–36.